Low-multipolarity magnetic transitions in ^{30}Si, ^{32}S, and ^{34}S studied by 180° electron scattering

M. Petraitis, J. P. Connelly,* Hall Crannell, L. W. Fagg, J. T. O'Brien,† and D. I. Sober
Department of Physics, The Catholic University of America, Washington, District of Columbia 20064

J. R. Deininger and S. E. Williamson
Department of Physics and Nuclear Physics Laboratory, University of Illinois, Urbana-Champaign, Illinois 61801

R. Lindgren
Department of Physics, University of Virginia, Charlottesville, Virginia 22901

S. Raman
Oak Ridge National Laboratory, Oak Ridge, Tennessee 37831
(Received 24 August 1993)

Low-multipolarity magnetic transitions of ^{30}Si, ^{32}S, and ^{34}S were studied by 180° inelastic electron scattering at low momentum transfers ($q \sim 0.3$–0.5 fm^{-1}). These measurements, made in the excitation energy region from 9 to 14 MeV, revealed several previously unreported levels. These are the first low-q results obtained by electron scattering for ^{30}Si and ^{34}S. Multipolarities and transition strengths for all the observed transitions were determined in a model-independent analysis. A large fragmentation of $M1$ strength is observed in the $4N + 2$ nuclei ^{30}Si and ^{34}S, while more strength is concentrated into fewer transitions in the self-conjugate nucleus ^{32}S. The experimental $M1$ strength distributions are compared with configuration-mixing shell-model calculations. The sums of the transition strengths are in good agreement with recent shell-model calculations using an effective $M1$ operator.

PACS number(s): 25.30.Dh, 23.20.Js, 27.30.+t

I. INTRODUCTION

The properties of low-multipolarity magnetic transitions, particularly magnetic dipole ($M1$) transitions, in the region of the *sd* shell in nuclei have been extensively studied for a number of years. The motivation for these studies arises from the relative simplicity and selectivity of the $M1$ operator, and the ability to perform calculations for these nuclei within a shell model that includes a large number of the available basis states. This subject has been extensively reviewed by Brown and Wildenthal [1] and Raman *et al.* [2].

Many of the predictions of the shell-model calculations have been tested in experiments. As one example, magnetic dipole strengths in ^{20,22}Ne, ^{24}Mg, ^{28,30}Si, and ^{32,34}S have been measured by nuclear resonance fluorescence (NRF) [3] and compared with a set of systematic shell-model predictions [4]. These authors find reasonable agreement between theory and experiment as to the average excitation energy of magnetic dipole transitions. They have also observed that the introduction of configuration mixing into the shell model reduces the predicted sum of $M1$ strength, and greatly reduces the discrepancy between calculation and experiment, especially for the even-even self-conjugate ($4N$) nuclei.

There remains, however, a long standing problem that the total $M1$ transition strength measured in experiments is typically only 60–80 % of that predicted. This discrepancy may well be due to effects of higher-order configuration mixing, isobaric excitations, and meson exchange currents, not explicitly included in the calculations performed to date. This problem has been addressed in part by Brown and Wildenthal [5] in a procedure in which they introduce phenomenological and empirically determined effective $M1$ operators into the shell-model calculations. They obtained a parametrization for effective $M1$ operators by a global fit to all magnetic moments and $M1$ transition matrix elements in the range $A = 17$–39 for which precisely determined values were available. To the extent that the effects due to terms not included in the shell-model calculations are slowly varying functions of the atomic number, this technique offers a relatively simple procedure for predicting the properties of as yet unmeasured $M1$ transitions. The efficacy of this technique can be tested by comparing predictions to data not included in the original empirical fit.

A combined analysis of both electromagnetic and hadronic cross sections has been made for ^{24}Mg by Richter *et al.* [6]. Experimental results are found to be

*Present address: The George Washington University, Washington, DC 20052.
†Permanent address: Montgomery College, Rockville, MD 20850.

in good agreement with the expectations based on calculations using the empirical effective operator obtained by Brown and Wildenthal [5], and using the effective operator from direct theoretical calculations of Towner and Khanna [7]. These findings seem to confirm the importance of meson exchange currents (MEC) in nuclei. Extending such studies in the future to other regions of the *sd* shell could confirm their findings and test theoretical calculations.

While a great deal of data has been accumulated on $M1$ transitions in even-even nuclei in the lower *sd* shell ($A \leq 28$), data on nuclei in the upper *sd* shell are much more limited. This is especially true for $4N + 2$ nuclei, where two neutrons are added to the $4N$ core. For $4N + 2$ nuclei, the strengths of single-particle transitions are found to be, on the average, only 20–50 % of those in $4N$ nuclei [3]. In addition, previous data have failed to reveal several predicted strong $M1$ transitions. For example, only 21% of the $M1$ strength predicted in ^{34}S was detected in the NRF experiments. The NRF experiments can only detect dipole transitions that are below the particle emission threshold, which is at 10.9 MeV in the case of ^{34}S. The large missing strength in ^{34}S would be explained if the strong $M1$ excitation predicted by the shell-model calculation at 10.02 MeV instead occurs above this energy.

Electron scattering experiments can provide data on dipole transitions above the nucleon threshold, as well as data on higher multipolarity transitions, data which are unavailable from NRF experiments. In the work reported here low-multipolarity magnetic transitions were excited by 180° electron scattering on ^{30}Si, ^{32}S, and ^{34}S as part of a continuing study of the upper *sd*-shell nuclei. These results are the first obtained at low momentum transfer for ^{30}Si, and the first at any momentum transfer for ^{34}S.

Measurements were made for momentum transfers between 0.3 and 0.5 fm^{-1}, in the excitation energy range from 9 to 14 MeV. Data were taken on ^{32}S principally to measure background caused by the presence of ^{32}S in the ^{34}S target, but they provide useful supplementary measurements to those reported previously by Burt *et al.* [8].

In the following section relevant details of the experiment are described. Section III contains an outline of the data analysis techniques, and further details can be found in Ref. [9]. Procedures to determine transition multipolarities and strengths are described in Sec. IV and the results presented in Sec. V. The experimental results are then compared with shell-model calculations using both free-nucleon and effective $M1$ operators, and sum rules in Secs. VI and VII, respectively; these comparisons are followed by the conclusions in Sec. VIII. Tables of experimental cross sections are presented in the Appendix.

II. EXPERIMENT

The experiment was performed at the 180° electron scattering facility designed, constructed, and installed by the Catholic University of America (CUA) intermediate energy nuclear group at the Nuclear Physics Laboratory (NPL) of the University of Illinois at Urbana-Champaign. The design, installation, and performance history of this system are fully described by O'Brien *et al.* [10]. A dipole, called the separating magnet, located immediately in front of the target served to steer the incident beam onto the target and to deflect 180° scattered electrons into the momentum-analyzing spectrometer. This arrangement required that the target be shifted downstream from its normal position, which introduced the need for software corrections to the scattered electron momentum data as described below.

The electron beam used for this experiment was provided by MUSL-2 (microtron using a superconducting linac 2), a superconducting, 100% duty-cycle accelerator at NPL. The beam energies used in this work ranged from 28 to 64 MeV, and the beam current varied between 1 and 8 μA. The energy spread of this beam was typically on the order of 0.01%.

A thin (25.3-mg/cm^2) ^{30}Si target was supplied by the University of Virginia for the experiment. Sulfur targets, however, presented a greater difficulty. Because pure sulfur has a low melting point, it cannot be used in the beam without complicated cooling arrangements. Because of the inherent difficulty associated with gas targets, solid sulfur compounds were preferred. Li_2S used in the earlier experiment [8] is extremely hygroscopic and hence CaS was selected. Enriched CaS powder (with 95% of sulfur being ^{34}S by weight) and natural CaS (with the natural abundance of 95% ^{32}S) were supplied by the Oak Ridge National Laboratory. The powder was pressed into self-supporting 0.96-cm-diam wafers 25.0 mg/cm^2 thick, and placed between thin (0.013-cm) Be foils to be used as targets.

Data were collected as part of two experimental runs, each of around 3.5 weeks duration. During the first run, data were obtained for the ^{30}Si target at incident energies of 63.4, 53.2, 42.9, 33.0, and 32.8 MeV at 180°. Data at an angle of 135° , where longitudinal contributions are expected to be significant, were also obtained at an incident energy of 56.9 MeV. The energy and angle were chosen so as to match the momentum transfer for the 53.2-MeV 180° data. During the second run, incident energies of 56.5, 54.6, 45.7, 34.9, and 28.4 MeV were used to obtain data at 180° for ^{30}Si, ^{34}S, and ^{32}S targets. Data were also obtained at an angle of 149° using ^{34}S and ^{32}S targets with an incident energy of 56.5 MeV to match the q at the 180° data at 54.6 MeV.

The momentum acceptance of the spectrometer was limited to ±3% because of focal-plane instrumentation. Hence, an inelastic spectrum comprising the entire excitation region to be studied required four or five segments at different spectrometer settings. The excitation region was divided into suitable overlapping momentum intervals, and the spectrometer angle, spectrometer field, and separating magnet angle were set appropriately for each region. After the 180° data were taken, the separating magnet was removed from the scattering chamber, the target was moved upstream from its 180°-mode position to the center of the scattering chamber, and data were taken at the less backward scattering angle.

III. DATA ANALYSIS

In the normal, non-180° mode of operation, the momentum was calculated using the spectrometer field, and the fine-channel position along the focal plane was measured with a vertical-drift wire chamber. At 180° the target was no longer at the object point of the spectrometer focal-plane detector array, and the magnetic optics were substantially altered by the presence of the separating magnet. This effect required focal-plane software corrections described in Ref. [10] to obtain acceptable energy resolution.

Raw-event data were scanned to obtain histograms of reconstructed momentum, and the histograms were then converted into a format that could be read by the fitting program. The spectra were fitted using ALLFIT a versatile fitting program that has been routinely used to analyze data for electron scattering and several other reactions.

In each segment, which consisted of one momentum interval, a strong and clearly resolved peak was selected, and the parameters that gave the best fit to this peak shape were determined. These parameters were then used for the rest of the segment, with only the heights and positions of the peaks treated as variables. The excitation-energy scale was calibrated with known levels. For closely spaced or unresolved peaks, the positions were fixed at an interval relative either to a known strong level or to each other. For weak peaks, only those that appear in at least three out of four spectra were fitted. For the final fit, all peaks were fixed in position, and only the heights were allowed to vary.

Figure 1 shows a sample spectrum of counts vs excitation energy. The data span one excitation energy segment, from 8.2 to 10.6 MeV for the ^{30}Si target at an incident energy of 54.6 MeV. The typical energy resolution, full width at half maximum (FWHM), is around 100 keV, dominated mainly by target thickness. The spectrum shows four peaks known previously from NRF experiments [3], which were fitted to be at 8.94, 9.36, 9.77, and 10.48 MeV, respectively. The overall precision in the determination of excitation energy of the peaks observed in this work was ± 10 keV. Three additional peaks are also observed at 8.26, 9.96, and 10.27 MeV. Figure 2 shows data from both the enriched and natural CaS targets. The previously known Ca transitions at 9.87 and 10.32 MeV are seen in both spectra. The prominent $M1$ transition in ^{32}S at 11.16 MeV and the $M1$ transitions in ^{34}S at 9.48, 10.18, and 10.43 MeV can also be seen along with several weaker levels in each spectrum. The excitation energies obtained from NRF data and the Ca 10.32-MeV transition, were used in calibrating the excitation energy scale.

To determine the complete peak areas, the contributions of the radiation tails, calculated with standard formulas for (e,e') radiative correction functions, were extrapolated beyond the high-excitation-energy side of the fitting region of each peak. The statistical error based on raw counts for each peak was determined. A "formal fitting error" corresponding to the percent error in the peak area using the error matrix, was also obtained. Because of the relatively restricted range of momentum in each segment, obtaining an accurate estimate of the background was difficult. To estimate the contribution to the uncertainty in the peak area caused by uncertainty in the background, plausible low- and high-background functions for a number of the spectrum segments were chosen independently by five of the authors. These segments were then fitted with both the low and high background functions and the cross sections for the peaks extracted. The uncertainties deduced by comparing the cross sections extracted in this manner were about twice the formal fitting error, independent of the size of the peak. Because the uncertainty in the background subtraction appear largely uncorrelated from energy to energy, the uncertainty used in the following analysis is twice the formal fitting uncertainty deduced from the fitting procedure. An additional uncertainty of 6% has been added in quadrature to account for uncertainties in charge determination, fluctuations in detector efficien-

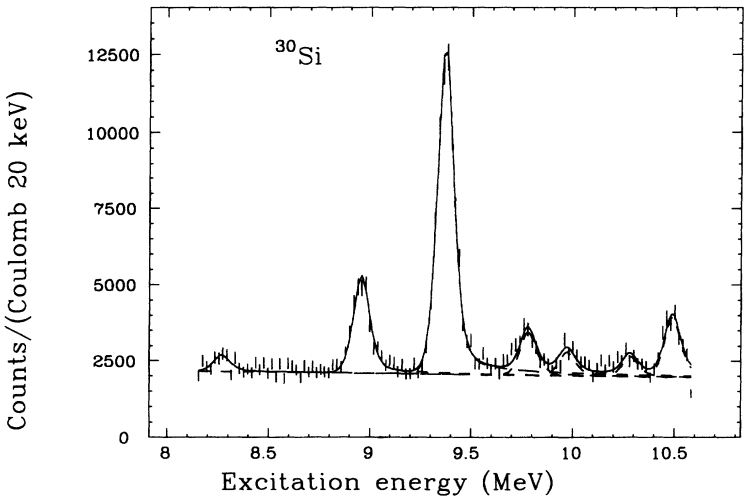

FIG. 1. A sample fitted spectrum showing data at 54.6-MeV incident energy for ^{30}Si. The solid line shows the total fit; the dashed line indicates the fitted background.

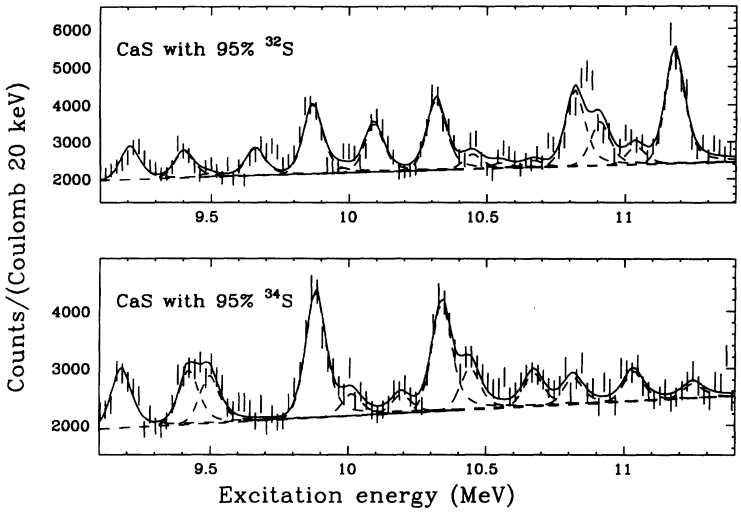

FIG. 2. Spectra showing data for both natural (top) and enriched (bottom) CaS targets at 56.5 MeV incident energy. As in Fig. 1, the solid line shows the total fit; the dashed line indicates the fitted background.

cies, and target thickness. Any inclusion of systematic uncertainties such as uncertainties in solid angle, Faraday cup efficiency, and absolute thickness of target were considered to be insignificant relative to the statistical and random uncertainties in the cross sections.

IV. TRANSITION MULTIPOLARITIES AND STRENGTHS

Using a "model-independent" analysis, applicable in electron scattering at low momentum transfers, transition multipolarities and strengths were determined for all observed levels. In the plane wave Born approximation (PWBA), the electric and magnetic cross sections can be written [11] in terms of the reduced transition probabilities $B(X\lambda,q)$ ($X = C$ Coulomb, E electric, or M magnetic) for the inelastic transition of multipolarity λ, from the ground state of spin J_i to a final state of spin J_f as

$$\left(\frac{d\sigma}{d\Omega}\right)_{E\lambda} = \alpha^2 a_\lambda q^{2\lambda} k_0^{-2} \left[\lambda(\lambda+1)^{-1} B(C\lambda,q) V_L(\theta) + B(E\lambda,q) V_T(\theta)\right] \eta^{-1}, \quad (1)$$

$$\left(\frac{d\sigma}{d\Omega}\right)_{M\lambda} = \alpha^2 a_\lambda q^{2\lambda} k_0^{-2} B(M\lambda,q) V_T(\theta) \eta^{-1}. \quad (2)$$

In these equations α is the fine-structure constant, $a_\lambda = 4\pi\lambda^{-1}[(2\lambda+1)!!]^{-2}$, $k_0 = E_0/\hbar c$ where E_0 is the incident energy, and the recoil factor is given by $\eta = 1 + (E_0/Mc^2)(1-\cos\theta)$, where M is the mass of the target nucleus and θ is the scattering angle.

If E_0 is large compared to the electron rest energy, the functions $V_L(\theta)$ and $V_T(\theta)$ can be written

$$V_L(\theta) = \tfrac{1}{2}(1+\cos\theta)/(y-\cos\theta)^2, \quad (3)$$

$$V_T(\theta) = \tfrac{1}{4}(2y+1-\cos\theta)/[(y-\cos\theta)(1-\cos\theta)], \quad (4)$$

where $y = 1+[E_x^2/2E_0(E_0-E_x)]$ and E_x is the excitation energy.

Examining Eq. (3) it can be seen that at 180° the longitudinal contribution vanishes, leaving only the transverse part. For a magnetic transition of multipolarity λ, the cross section at 180° is

$$\left(\frac{d\sigma}{d\Omega}\right)_{M\lambda} = \tfrac{1}{4}\alpha^2 a_\lambda q^{2\lambda} k_0^{-2} B(M\lambda,q)\eta^{-1}, \quad (5)$$

with $V_T = 1/4$. Unfortunately, because of the finite solid angle the data actually span a range of angles from approximately 177° to 180°; the average effective angle is therefore 178.5°. To check for contributions from strong longitudinal transitions over this extended acceptance, data were taken at a matched q point at a forward angle, where V_L is large, and used to determine whether a detectable longitudinal contribution was present.

In the PWBA, the measured $B(X\lambda,q)$ can be extrapolated to $q=\omega$, the so-called "photon point," in a fairly model-independent way. For small q, the reduced transition probabilities $B(C\lambda,q)$ and $B(M\lambda,q)$ are written in a power series in q :

$$\left[\frac{B(C\lambda,q)}{B(C\lambda,0)}\right]^{\frac{1}{2}} = 1 - \frac{q^2}{2(2\lambda+3)}R_{\rm tr}^2 + \frac{q^4}{8(2\lambda+3)(2\lambda+5)}R^{\star 4} - \cdots, \quad (6)$$

$$\left[\frac{B(M\lambda,q)}{B(M\lambda,0)}\right]^{\frac{1}{2}} = 1 - \frac{q^2}{2(2\lambda+3)}\frac{\lambda+3}{\lambda+1}R_{\rm tr}^2 + \frac{q^4}{8(2\lambda+3)(2\lambda+5)}\frac{\lambda+5}{\lambda+1}R^{\star 4} - \cdots, \quad (7)$$

where the "transition radii" $R_{\rm tr}$ and $R^\star$ are defined in

Ref. [12]. Using these equations, low-q data can be used to determine both multipolarity and transition strength $B(M\lambda, q=\omega)$. The extrapolation of the data to the photon point gives the $B(M\lambda, q=\omega)$ value. The experimental cross sections were corrected for Coulomb distortion by obtaining ratios of DWBA to PWBA cross sections using the code DENS [13]. These corrections ranged from 1.0 to 1.4.

The usual procedure followed in low-q electron scattering [14] is to assume a definite multipolarity λ and calculate $[B(M\lambda,q)]$ using Eq. (5), and plot $[B(M\lambda,q)]^{\frac{1}{2}}$ vs q^2. Only if the assumed multipolarity is correctly identified will such a plot show a linear relationship at low q, as dictated by the above equations. This procedure was performed for both $\lambda = 1$ and 2, first assuming a transverse magnetic and then a longitudinal electric transition, and tested for best agreement with Eqs. (6) and (7) with a reasonable transition radius ($R_{\rm tr} \simeq R_{\rm rms}$, the ground state rms charge radius). The data acquired in this work are neither of sufficient precision nor range to reliably extract three parameters. Therefore the term R^{*4} was set to be $1.14(R_{\rm tr}^2)^2$, the coefficient 1.14 obtained from theoretical distorted wave Born approximation (DWBA) calculations. Hence a least-squares fit of Eq. (7) to the 180° data was performed with two variables, $B(M\lambda,0)$ and the transition radius $R_{\rm tr}$, for each λ. A similar fit was calculated assuming a longitudinal transition.

One example of such fits is shown in Fig. 3 which illustrates the fits to the 11.16-MeV transition in ^{32}S. The upper two plots [Figs. 3(a) and (b)] assume magnetic dipole ($M1$) and magnetic quadrupole ($M2$) transitions, respectively, while the lower two [Figs. 3(c) and (d)] assume $C1$ and $C2$ transitions, respectively. The data at the more forward q-matching angle are plotted as triangles, while the 180° points are plotted as crosses, with the filled-in-square indicating $[B(X\lambda,\omega)]^{\frac{1}{2}}$. The radius $R_{\rm tr}$ and $B(X\lambda,\omega)$ are printed at the top of each plot. Because the q-matching value agrees with the value at 180° for the $M1$ and $M2$ assignments, and not for the $C1$ and $C2$ cases, the transition is seen to be transverse. The fit for the $M1$ assumption has a reasonable radius and χ^2, while the fit assuming a $M2$ transition has an unreasonably high radius (6.01 fm). Hence, an assignment of $M1$ is made for this transition.

If the fitted $R_{\rm tr}$ were implausible ($R_{\rm tr} \gg$ or $\ll R_{\rm rms}$), the fit was repeated varying only $B(X\lambda,0)$ using a reasonable fixed radius, $R_{\rm tr}$= 3.1 and 3.4 fm for Si and S, respectively, for λ=1, and $R_{\rm tr}$ = 4.0 fm for λ=2. Then a multipolarity assignment was made choosing the best fit. Based on this analysis, it appeared that unresolved doublets existed in some of the data. Such data were therefore fitted with fixed radii to include two multipolarities

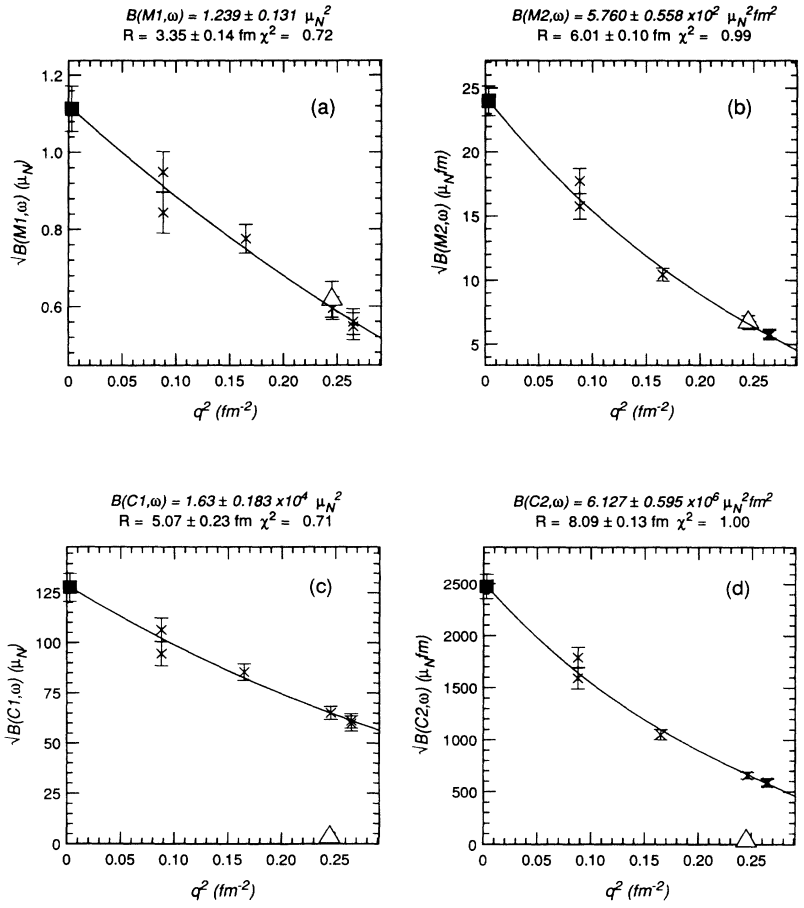

FIG. 3. Fits for the 11.16-MeV transition in ^{32}S assuming $M1$ (a), $M2$ (b), $C1$ (c), and $C2$ (d) assignments for the transition.

with a varying ratio of mixture and tentative assignments were made.

V. RESULTS

The strong, well-known $M1$ transition in ^{40}Ca at 10.32 MeV was useful in checking the normalization of our data. The values of $B(M1,\omega)$ obtained from our experiment, $(1.17\pm0.11)\mu_N^2$ from the enriched CaS data and $(0.94\pm0.12)\mu_N^2$ from the natural CaS data, are in good agreement with the values of $(1.12\pm0.07)\mu_N^2$ published by Gross *et al.* [15] and $(1.04\pm0.08)\mu_N^2$ by Burt *et al.* [16].

Table I gives the observed transitions in ^{30}Si along with the most probable multipolarity assignments and transition strengths. A "†" indicates the presence of observed longitudinal strength. A "grade" was chosen to indicate the degree of confidence in the multipolarity assignment. A grade of " ⋆⋆⋆ " shows an isolated strong transition for which a confident multipolarity assignment has been made. A " ⋆⋆ " indicates a most likely multipolarity assignment, but factors such as a high χ^2 in the fit, presence of considerable longitudinal strength, or inadequate resolution of low-q data, indicate a weak possibility of other multipolarity mixtures. A " ⋆ " indicates a very weak or not totally resolved transition with a questionable assignment. Other than the transitions listed in the table, peaks were observed at 7.27, 7.67, and 8.28 MeV in the data at an incident energy of 63.4 MeV. These could correspond to the transitions at 7.256 (1^+), 7.668 $(1,2)^+$, and 8.290 $(1^- - 4^+)$ listed in the data tables of Endt [17]. None of these transitions were observed in NRF data, which suggests that these could be $M2$ transitions — especially the strong peak at 7.67 MeV.

The data from both CaS targets were analyzed independently, and the calcium transitions were identified and eliminated from the sulfur analyses by comparing both sets of data and checking with earlier high-resolution electron scattering data on ^{40}Ca [18,19]. Results for ^{40}Ca determined from these data have been reported in Ref. [9].

Tables II and III give the excitation energies of the observed transitions and the most probable multipolarity assignments and transition strengths for ^{32}S and ^{34}S respectively, with notation similar to that in the previous table. Some peaks were seen in the data at only one or two incident energies; for these a multipolarity determination was not possible using the data analysis given

TABLE I. Magnetic dipole ($M1$) and quadrupole ($M2$) strengths in ^{30}Si. The second column gives the most probable assignment, with the confidence in the assignment represented by the grade in column 7. Where the multipole assignment is uncertain, the less probable assignment is enclosed in parentheses. A "†" indicates presence of considerable longitudinal strength. Column 3 shows the transition radius used in the fit and column 6 gives the χ^2 per degree of freedom of the fit.

E_x (MeV)	λ	R_{tr}	$B(M1,\omega)$ (μ_N^2)	$B(M2,\omega)$ $(\mu_N^2$ fm$^2)$	χ^2	Grade
8.94	$M1$	2.74	0.33 ± 0.03		0.55	⋆⋆⋆
9.36	$M1$	3.12	1.52 ± 0.07		0.96	⋆⋆⋆
9.77	$M1$	2.93	0.23 ± 0.02		2.85	⋆⋆
9.96	$M2$	4.80		20 ± 6	1.29	⋆⋆
10.27	$M2$ $(M1)$ †	4.00		15 ± 2	2.20	⋆
10.48	$M1$	3.29	0.37 ± 0.03		1.03	⋆⋆⋆
10.62	$M1$	3.10	0.13 ± 0.01		4.02	⋆⋆
10.76	$M1$†	3.00	0.08 ± 0.02		0.40	⋆
10.93	$M2$	4.60		20 ± 6	0.16	⋆⋆
11.18	$M2$	4.16		12 ± 4	1.81	⋆
11.36	$M1$	3.25	0.11 ± 0.02		2.92	⋆
11.70	$M1$	3.44	0.09 ± 0.02		1.36	⋆⋆
11.84	$M2$	4.84		22 ± 6	2.41	⋆⋆
12.02	$M2$	4.92		33 ± 7	2.27	⋆⋆
12.20	$M1$	3.21	0.10 ± 0.02		0.35	⋆
12.40	$M2$	4.23		24 ± 6	1.19	⋆⋆
12.70	$M2$	5.10		30 ± 8	2.11	⋆
12.83	$M2$	4.47		21 ± 7	4.73	⋆
13.03	$M1$	3.53	0.10 ± 0.03		0.91	⋆⋆
13.14	$M2$	3.20		20 ± 4	1.48	⋆
13.40	$M2$ †	4.00		30 ± 2	3.72	⋆⋆
13.60	$M1$	3.79	0.09 ± 0.03		1.93	⋆⋆
13.79	$M1+M2$	3.1	0.50 ± 0.05	47 ± 12	0.78	⋆⋆
14.00	$M2$	4.72		36 ± 13	2.49	⋆⋆
14.20	$M2(M1)$	4.00		18 ± 3	3.58	⋆
14.63	$M1(M2)$	3.10	0.11 ± 0.02		0.61	⋆

TABLE II. Magnetic dipole ($M1$) and quadrupole ($M2$) strengths ^{32}S. Notation as in Table I.

E_x (MeV)	λ	$R_{\rm tr}$	$B(M1,\omega)\,(\mu_N^2)$	$B(M2,\omega)\,(\mu_N^2\,{\rm fm}^2)$	χ^2	Grade
9.66	$M1$	3.86	0.55 ± 0.24		0.06	⋆⋆
9.98	$M1$	3.40	0.09 ± 0.04		0.84	⋆
10.09	$M2$	4.64		68 ± 30	0.28	⋆⋆⋆
10.45	$M1$	3.30	0.10 ± 0.08		1.75	⋆
10.81	$M2$	4.23		103 ± 26	2.22	⋆⋆
10.90	$M1(M2)$	3.40	0.33 ± 0.04		0.77	⋆
11.16	$M1$	3.36	1.24 ± 0.13		0.76	⋆⋆⋆
11.50	$M1$	3.40	0.10 ± 0.04		0.83	⋆⋆
11.65	$M1$†	3.24	0.77 ± 0.14		2.85	⋆⋆
11.88	$M2$	4.00		24 ± 5	0.43	⋆
12.03	$M2(M1)$	4.00		26 ± 6	1.00	⋆
12.19	$M1$	2.32	0.14 ± 0.09		0.26	⋆
12.65	$M1$	3.40	0.11 ± 0.04		0.67	⋆⋆
12.98	$M1$	3.40	0.07 ± 0.04		0.20	⋆
13.41	$M1(M2)$	3.40	0.54 ± 0.06		4.27	⋆⋆
13.78	$M1$	3.40	0.39 ± 0.05		0.26	⋆
13.97	$M1(M2)$	2.42	0.20 ± 0.11		0.77	⋆
14.45	$M1$	3.40	0.18 ± 0.05		0.40	⋆
14.77	$M2$	4.00		26 ± 6	0.35	⋆

TABLE III. Magnetic dipole ($M1$) and quadrupole ($M2$) strengths in ^{34}S. Notation as in Table I.

E_x (MeV)	λ	$R_{\rm tr}$	$B(M1,\omega)\,(\mu_N^2)$	$B(M2,\omega)\,(\mu_N^2\,{\rm fm}^2)$	χ^2	Grade
9.48	$M1$	3.40	0.58 ± 0.05		1.11	⋆⋆
9.87	$M1$	3.40	0.25 ± 0.07		0.43	⋆⋆
10.00	$M1$	3.40	0.19 ± 0.04		1.29	⋆
10.18	$M1$	4.33	0.66 ± 0.12		1.66	⋆⋆
10.43	$M1$	3.40	0.21 ± 0.04		1.52	⋆⋆
10.66	$M1(M2)$	3.40	0.16 ± 0.05		0.10	⋆
10.80	$M1$†	3.48	0.26 ± 0.09		1.56	⋆⋆
11.02	$M1$	2.69	0.11 ± 0.06		1.08	⋆
11.35	$M1$	3.40	0.20 ± 0.04		1.23	⋆⋆
11.50	$M1$	3.40	0.23 ± 0.04		2.52	⋆⋆
12.12	$M1$	3.10	0.25 ± 0.12		0.12	⋆⋆
12.18	$M2$	4.00		46 ± 5	0.86	⋆⋆
12.46	$M1(M2)$	3.4	0.16 ± 0.05		0.28	⋆⋆
12.66	$M1$	3.21	0.39 ± 0.11		1.18	⋆⋆⋆
12.93	$M2(M1)$	4.00		16 ± 5	0.33	⋆
13.59	$M2$	3.70		31 ± 22	0.73	⋆
13.79	$M2$	4.00		18 ± 5	0.38	⋆
13.99	$M1$	3.42	0.13 ± 0.10		0.32	⋆⋆
14.20	$M1(M2)$	3.40	0.12 ± 0.05		0.80	⋆
14.32	$M2(M1)$	4.00		32 ± 6	3.32	⋆
14.43	$M1(M2)$	3.40	0.27 ± 0.05		0.25	⋆
14.80	$M2$	4.00		90 ± 7	0.70	⋆⋆

TABLE IV. Comparison of current results with results from NRF experiments for ^{30}Si.

	This work		NRF (Ref. [3])	
E_x (MeV)	λ	$B(M1,\omega)\,(\mu_N^2)$	λ	$B(M1,\omega)\,(\mu_N^2)$
8.943	1^+	0.33 ± 0.03	1^+	0.69 ± 0.22
9.357	1^+	1.52 ± 0.07	1^+	2.21 ± 0.54
9.768	1^+	0.23 ± 0.02	1^+	0.33 ± 0.14
10.478	1^+	0.37 ± 0.03	1^+	0.35 ± 0.14

TABLE V. Comparison of current results with results from earlier (e,e') (Ref. [8]) and NRF experiments (Ref. [3]) for ^{32}S.

	This work		(e,e') (Ref. [8])		NRF (Ref. [3])	
E_x (MeV)	λ	$B(M1,\omega)(\mu_N^2)$	λ	$B(M1,\omega)(\mu_N^2)$	λ	$B(M1,\omega)(\mu_N^2)$
9.66	1^+	0.55 ± 0.24	1^+	0.69 ± 0.18	1^+	0.43 ± 0.12
10.09	2^-		(1^+)			
10.81	2^-		(2^-)			
11.16	1^+	1.24 ± 0.13	1^+	2.40 ± 0.22		
11.65	1^+	0.77 ± 0.14	1^+	1.26 ± 0.20		

in the previous section. They include for ^{32}S a peak at 9.21 MeV which was observed in NRF experiments [3] and which was not observed in earlier electron scattering [8]. A 1^+ transition at 9.290 MeV, which is mentioned in Ref. [17], was not detected in our data. Data for ^{34}S at incident energies of 56.5 and 54.5 MeV show peaks at 8.20, 8.67, and 9.17 MeV. These could correspond to transitions listed at 8.185 (1^+), 8.651 (1^+), and 9.158 $(1,2)^+$ in Ref. [17]. Only the first two transitions were seen in NRF experiments, thus suggesting that the transition at 9.158 MeV is a $M2$ transition.

Tables IV–VI compare the present results for ^{30}Si, ^{32}S, and ^{34}S with the results from NRF experiments [3]. Table V also includes the results from the earlier (e,e') experiment on ^{32}S [8]. The data obtained for ^{30}Si are considerably more precise than the earlier NRF experiments. Though the current $B(M1)$ values for ^{30}Si (see Table IV) appear systematically lower than the NRF results, the two sets of values are consistent if the large uncertainties in the NRF measurements are taken into account. For ^{34}S, our results are all a factor of about 2 higher than the NRF results. The reason for this disagreement is not understood. The (e,e') results for ^{32}S presented in Table V show general agreement, except for the 11.16-MeV state, where the current result for the transition strength is a factor of 2 lower, with 10% quoted uncertainties, than the previous electron scattering result. Figure 4 shows data from the current work as well as data from Burt *et al.* [8] for this 11.16-MeV transition. Data from Ref. [8] are represented by solid squares and triangles, indicating data taken at 180° and 162.4°, respectively. The 180° data from Burt *et al.* [8] are in good agreement with the data obtained from this work, while the 162.4° data, from Burt *et al.* [8] clearly leads to a higher value for the strength for this transition. The disagreement with the 162.4° data could be due to the presence of additional longitudinal strength due to an unresolved state at this more forward angle.

VI. COMPARISON WITH SHELL-MODEL CALCULATIONS

Shell-model calculations of the $M1$ strength distributions for the nuclei under study were obtained from Brown [20]. Results of calculations using the free-nucleon operator as well as an empirical effective $M1$ operator [5] were used to compare with the current experimental results. Figures 5–7 show comparisons of the theoretical predictions of $M1$ strengths with the experimental results for ^{30}Si, ^{32}S, and ^{34}S, respectively, for the range of excitation energy covered by this experiment. The shell-model strengths using the effective $M1$ operator are shown in the upper part, and the experimental strengths appear in the lower part of each figure. The unshaded bars of the theoretical strengths are caused by $\Delta T = 0$ transitions and the shaded bars result from $\Delta T = 1$ transitions. The shaded bars in the experimental strengths represent data from earlier (e,e') [8] and NRF [3] experiments.

The locations of large $M1$ transitions are predicted well by the shell-model calculations for all the nuclei under study. In all three cases, calculations using the effective $M1$ operator improve the agreement between the predicted strengths and the experimental findings compared to calculations using free-nucleon operators. Because of statistical limitations of the data, transitions with strengths less than $\sim 0.08\mu_N^2$ could not be observed. Thus, the experimental measurements represent a lower limit on the total strength.

TABLE VI. Comparison of current results with results from NRF experiments for ^{34}S.

	This work		NRF (Ref. [3])	
E_x (MeV)	λ	$B(M1,\omega)\,(\mu_N^2)$	λ	$B(M1,\omega)\,(\mu_N^2)$
9.478	1^+	0.58 ± 0.05	1^+	0.30 ± 0.05
9.860	1^+	0.25 ± 0.07	1^+	0.15 ± 0.05
10.170	1^+	0.66 ± 0.07	1^+	0.25 ± 0.07
10.803	1^+	0.26 ± 0.09	$(1,2^+)$	0.12 ± 0.04

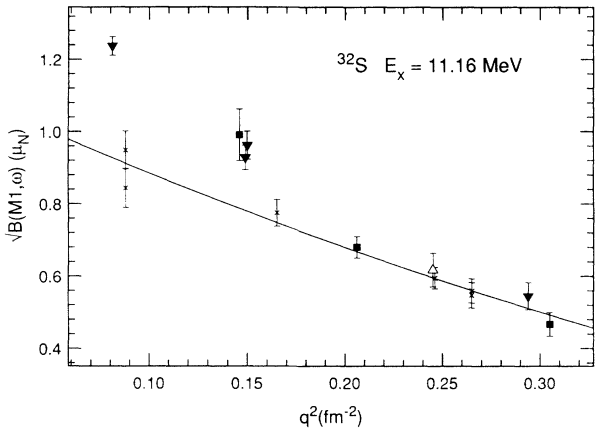

FIG. 4. Fit for the 11.16-MeV transition in ^{32}S showing data from current work and data from the previous electron scattering experiment [8]. Data from Ref. [8] are represented by solid squares and triangles, indicating data taken at 180° and 162.4°, respectively. The solid line indicates the fit to the current data.

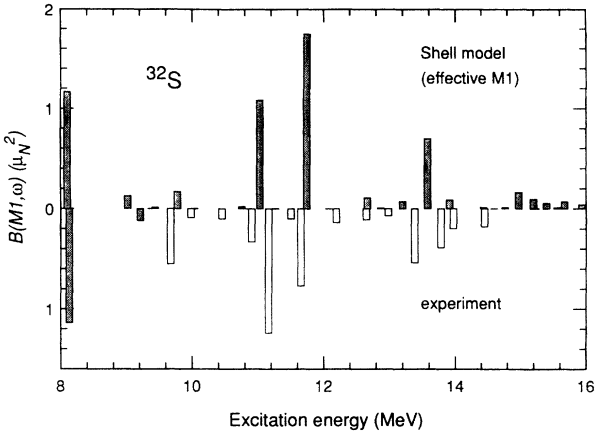

FIG. 6. Comparison of shell-model and experimental strengths for ^{32}S. The shaded bars in the shell-model strengths indicate $\Delta T = 1$ transitions. The shaded bars in the experimental strengths represent data from Refs. [3,8]. The unshaded bars are experimental results from the current work.

Figure 5 shows considerable fragmentation of $M1$ strength in ^{30}Si. For ^{34}S, as shown in Fig. 7, a large $M1$ strength ($2.87\mu_N^2$ with free-nucleon operators and $1.61\mu_N^2$ with effective $M1$ operators) is predicted near 10.2 MeV. Experimentally, it is seen to be fragmented into several levels, with two large $M1$ pieces observed at 9.48 and 10.18 MeV. The fragmentation is less severe in the case of the self-conjugate nucleus ^{32}S, which has a few larger $M1$ transitions.

The energy centroid of the $M1$ strength distribution and its rms width are defined as

$$\langle E_x \rangle = \sum E_x B(M1) \Big/ \sum B(M1), \tag{8}$$

$$\sigma_{E_x} = \left(\sum \{(E_x - \langle E_x \rangle)^2 B(M1)\} \Big/ \sum B(M1) \right)^{\frac{1}{2}}. \tag{9}$$

Table VII shows the centroids and widths of the experimental and shell-model results for the nuclei under study. The results from shell-model calculations were determined considering transitions only up to an excitation energy of 15 MeV. The experimental values for the centroid are in agreement with the results from shell-model

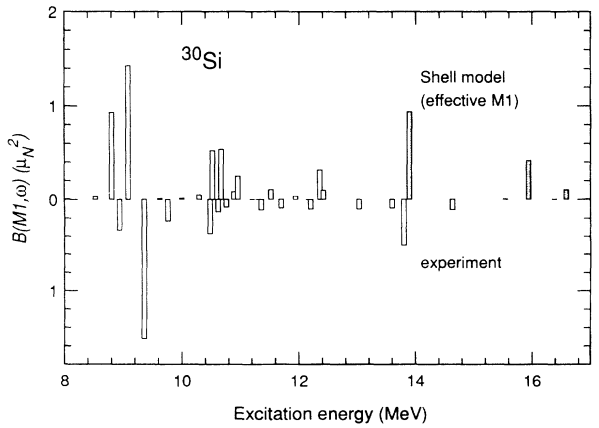

FIG. 5. Comparison of shell-model and experimental strengths for ^{30}Si. The shaded bars in the shell-model strengths indicate $\Delta T = 1$ transitions and the unshaded bars represent $\Delta T = 0$ transitions.

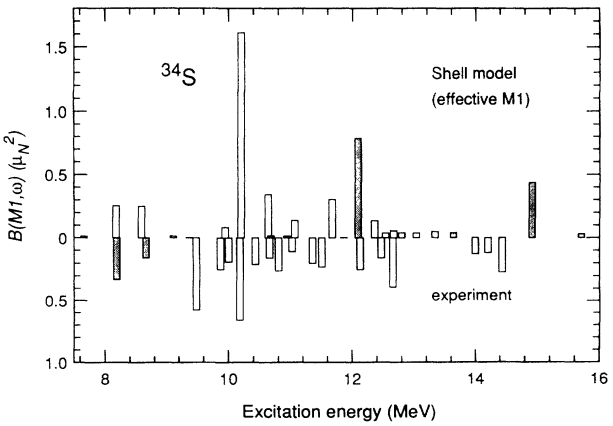

FIG. 7. Comparison of shell-model and experimental strengths for ^{34}S. The shaded bars in the shell-model strengths indicate $\Delta T = 1$ transitions and the unshaded bars represent $\Delta T = 0$ transitions. The shaded bars in the experimental strengths represent data from from Ref. [3]. The unshaded bars are experimental results from the current work.

TABLE VII. Energy centroids and widths for ^{30}Si, ^{32}S, and ^{34}S computed up to an excitation energy of 15 MeV.

Target		Current experiment	Shell-model results (Effective)	(Free)
^{30}Si	Energy centroid (MeV)	10.67	10.58	10.71
	rms width (MeV)	1.80	1.90	1.86
^{32}S	Energy centroid (MeV)	11.07	11.00	11.32
	rms width	1.90	2.00	1.85
^{34}S	Energy centroid (MeV)	10.92	10.92	11.09
	rms width (MeV)	1.69	2.05	2.02

calculations, while the experimental widths are almost everywhere narrower than the predicted values. This disagreement might be caused by the existence of weaker transitions below the experimental detection threshold.

VII. COMPARISON WITH SUM RULES

The summed experimental $M1$ strength can be compared with the shell-model calculations and theoretical sum rules. Figures 8–10 plot the "running sum" of experimental and theoretical $M1$ strengths up to $E_{\rm incr}$, where $E_{\rm incr}$ is the maximum excitation energy transition included in the sum.

For both ^{32}S and ^{34}S, the sums from the shell-model calculations using the effective $M1$ operator are in good agreement with the experimental sums, with ratios of $\sum B(M1)_{\rm expt}/\sum B(M1)_{\rm sm}$ equal to 1.08 and 0.97, respectively (see Table VIII). However, the experimental sums appear quenched to a large degree when compared with the calculations using the free-nucleon operator, the ratio being 0.73 and 0.56, respectively. For ^{30}Si the agreement with the effective $M1$ operator calculations is not as good with a ratio of 0.70, but again the strength appears even more quenched with the total strength only 0.45 of the shell-model value using free-nucleon operators. More strength could be present in the excitation energy ranges outside the region studied in this experiment. The missing $M1$ strength, as reported previously [3], especially in ^{34}S, has been largely accounted for as a result of the experimental findings reported here.

These data also can be compared with the results of an independent particle model (IPM) calculation. In the IPM, assuming a $d_{5/2} \rightarrow d_{3/2}$ $M1$ transition, the sum of the isovector and isoscalar $M1$ strengths is given by [21]

$$\sum B(M1,\omega) = \frac{9}{20\pi}\left[n_p(g_p^s - g_p^l)^2 + n_n(g_n^s - g_n^l)^2\right], \tag{10}$$

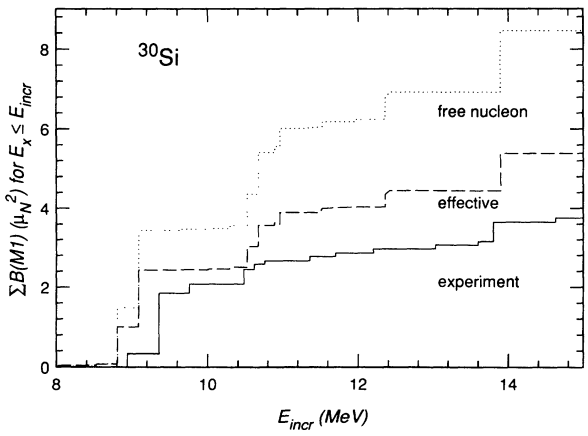

FIG. 8. Running sums of shell-model and experimental $M1$ strengths for ^{30}Si. The solid line shows the experimental sum and the shell-model calculation sums are indicated by dashed lines (using effective $M1$ operator) and dotted lines (using free nucleon operator).

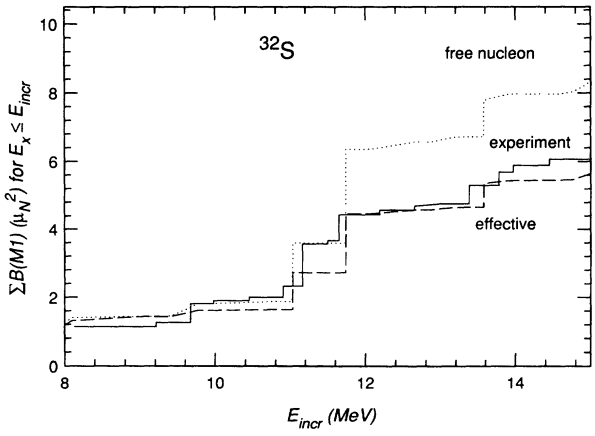

FIG. 9. Running sums of shell-model and experimental $M1$ strengths for ^{32}S. The solid line shows the experimental sum and the shell-model calculation sums are indicated by dashed lines (using effective $M1$ operator) and dotted lines (using a free-nucleon operator).

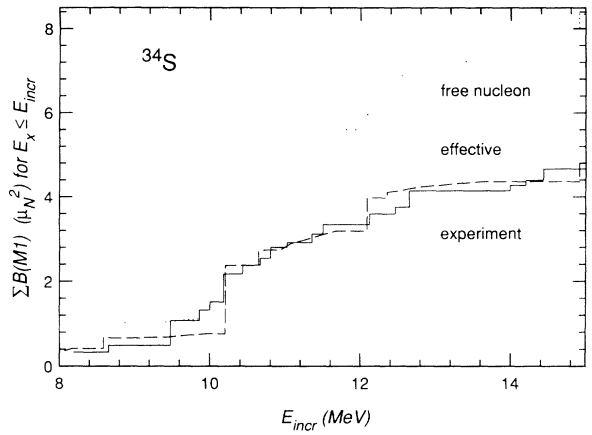

FIG. 10. Running sums of shell-model and experimental $M1$ strengths for ^{34}S. The solid line shows the experimental sum and the shell-model calculation sums are indicated by dashed lines (using effective $M1$ operator) and dotted lines (using a free-nucleon operator).

where n_p and n_n are the number of active (valence) proton and neutron particles or holes. This non-energy-weighted IPM sum rule gives a total sum of $M1$ strengths of $4.19\mu_N^2$ for ^{30}Si and ^{34}S and zero for ^{32}S, a closed subshell nucleus (see Table IX). The experimental sums, $\sum B(M1)$ are $3.76\mu_N^2$, $6.07\mu_N^2$, and $4.66\mu_N^2$ for the three nuclei ^{30}Si, ^{32}S, and ^{34}S, respectively. Configuration mixing seems to play an important role, especially in ^{32}S, which has a predicted total IPM sum of zero.

The Kurath sum rule for $\Delta T = 1$ transitions in $4N$ nuclei [22]

$$\sum_k \omega_k B(M1,\omega)\uparrow \cong -a\frac{3}{4\pi}\left[\mu_n - \mu_p + \tfrac{1}{2}\right]^2 \times\langle 0 \mid \sum_i \mathbf{l}(i)\cdot\mathbf{s}(i) \mid 0\rangle, \qquad (11)$$

gives total energy-weighted sums $\sum E_x B(M1)$ of 101 MeV μ_N^2 for ^{32}S and ^{30}Si and 76 MeV μ_N^2 for ^{34}S. The energy-weighted sums from experiment, and from shell-model calculations and Kurath sum rule are given in Table X. The shell-model sums are computed up to

TABLE VIII. Ratio $\sum B(M1)_{\rm exp}/\sum B(M1)_{\rm sm}$ for ^{30}Si, ^{32}S, and ^{34}S, where $\sum B(M1)_{\rm exp}$ and $\sum B(M1)_{\rm sm}$ are from the current experiment and shell-model calculations [18], respectively.

Target	$\sum B(M1)_{\rm exp}/\sum B(M1)_{\rm sm}$ (Effective)	(Free)
^{30}Si	0.70	0.45
^{32}S	1.08	0.73
^{34}S	0.97	0.56

TABLE IX. Summed $M1$ strengths [$\sum B(M1)$ in units of μ_N^2] for ^{30}Si, ^{32}S, and ^{34}S computed up to an excitation energy of 15 MeV.

	Experiment	Shell model (Effective)	(Free)	IPM sum rule
^{30}Si	3.76 ± 0.12	5.38	8.45	4.19
^{32}S	6.07 ± 0.39	5.63	8.29	0
^{34}S	4.66 ± 0.29	4.80	8.35	4.19

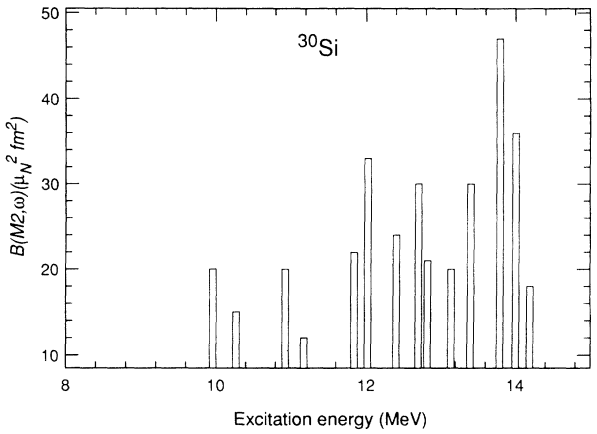

FIG. 11. Experimental $M2$ strength distribution in ^{30}Si.

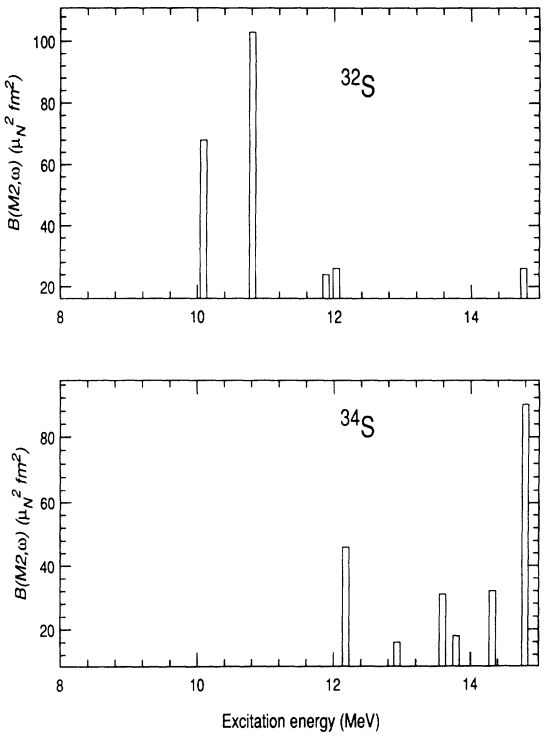

FIG. 12. Experimental $M2$ strength distribution in ^{32}S and ^{34}S.

TABLE X. Energy-weighted sum $\sum E_x B(M1)$ (MeV μ_N^2) for ^{30}Si, ^{32}S, and ^{34}S computed up to an excitation energy of 15 MeV.

Target	Experiment	Shell-model results (Effective)	Shell-model results (Free)	Kurath sum rule
^{30}Si	40.1 ± 17.4	57.0	90.6	101.3
^{32}S	67.2 ± 17.4	61.9	93.9	101.3
^{34}S	50.9 ± 12.0	52.4	92.6	76.0

TABLE XI. Cross sections (10^{-7} fm^2/sr) and uncertainties (%) for transitions in ^{30}Si. Upper limits are given for cases with large uncertainties.

	Incident energy E_0 (MeV)																	
E_x	63.4		54.6		53.2		45.7		42.9		34.9		33.0		32.8		56.9, 135°	
(MeV)	σ	$d\sigma$	σ	$d\sigma$	σ	$d\sigma$	σ	$d\sigma$	σ	$d\sigma$	σ	$d\sigma$	σ	$d\sigma$	σ	$d\sigma$	σ	$d\sigma$
8.94	1.39	14	2.36	10	1.94	16	2.96	8	3.36	19	4.08	8	4.17	13	3.44	16	0.91	19
9.36	4.08	9	7.92	7	4.07	9	11.55	6	8.14	8	18.08	6	11.85	9	14.99	7	16.95	7
9.77	1.01	19	1.05	17	1.36	22	1.91	10	3.30	20	2.11	11	3.43	14	3.77	18	1.49	31
9.96	0.40	42	0.58	27	0.52	48	0.31	39	0.97	58	0.64	28	1.15	50	0.84	51	<1.75	
10.27	0.58	30	0.46	35	0.35	68	0.68	19	<0.89		0.67	27	1.51	28	[a]		2.01	25
10.48	4.28	8	1.46	13	1.14	19	1.55	13	1.51	24	2.38	10	3.00	22	3.69	13	3.51	19
10.62	[a]		[a]		<0.48		0.37	40	1.07	56	1.61	13	2.31	18	1.20	63	[a]	
10.76	<0.28		0.48	34	0.54	57	0.62	25	<0.98		0.73	24	1.19	42	<1.34		2.63	20
10.93	0.49	36	0.54	30	0.54	57	0.69	23	0.96	58	0.55	31	<0.88		<1.30		0.86	56
11.18	0.20	92	0.26	58	0.50	36	0.39	37	0.48	38	0.35	49	0.53	58	0.64	87	1.38	35
11.36	0.44	48	0.16	97	0.47	46	<0.20		0.66	48	1.42	15	0.79	60	0.63	74	1.53	38
11.70	0.34	56	[a]		0.31	92	0.42	34	0.51	86	0.75	24	1.52	30	1.04	43	0.32	47
11.84	0.61	34	0.35	43	0.40	73	0.56	28	0.65	69	0.41	43	0.66	67	1.55	31	0.36	39
12.02	0.73	28	0.73	20	0.88	36	0.61	26	<0.64		1.08	17	1.29	34	0.52	74	0.46	33
12.20	0.31	60	0.32	43	0.63	47	0.80	21	0.79	58	1.00	20	[a]		0.83	50	<0.50	
12.40	0.93	22	0.71	21	1.12	28	0.69	24	0.88	66	0.93	21	<0.92		0.57	93	<0.89	
12.70	0.46	46	0.63	23	0.83	37	<0.21		0.94	47	0.66	28	0.94	53	1.25	41	<0.80	
12.83	0.69	32	0.61	24	1.04	31	0.15	99	0.78	56	0.19	97	1.81	27	0.81	59	0.62	77
13.03	<0.33		0.33	42	0.58	52	0.50	32	1.32	35	0.80	24	<1.10		1.24	38	1.73	28
13.14	0.36	45	1.22	14	1.29	19	0.88	20	1.40	24	0.98	18	0.96	47	1.51	34	0.95	64
13.40	1.79	14	0.77	18	1.51	22	0.83	20	1.27	29	1.11	16	1.11	38	1.43	47	1.23	49
13.60	[a]		0.23	57	0.50	58	0.28	55	0.53	59	0.44	36	0.45	93	1.71	36	1.60	36
13.79	2.50	12	4.55	8	4.13	12	5.38	7	4.66	11	5.63	7	6.64	11	5.88	11	6.80	11
14.00	[b]		1.08	16	1.24	29	0.75	22	1.21	40	[b]		[b]		1.36	30	2.91	18
14.19	[b]		0.74	22	1.04	33	<0.26		0.70	66	[b]		[b]		1.12	36	<1.44	
14.63	[b]		0.60	26	0.92	36	[b]		0.95	49	[b]		[b]		0.81	45	<0.84	

[a] Unable to extract cross section here.
[b] Outside range of spectra.

TABLE XII. Cross sections (fm^2/sr) and uncertainties (%) for transitions in ^{32}S. Upper limits are given for cases with large uncertainties.

	Incident energy E_0 (MeV)									
E_x	56.5		54.6		45.7		34.9		56.5, 149°	
(MeV)	$10^7\sigma$	$d\sigma$ (%)	$10^7\sigma$	$d\sigma$ (%)	$10^7\sigma$	$d\sigma$ (%)	$10^7\sigma$	$d\sigma$ (%)	$10^7\sigma$	$d\sigma$ (%)
9.66	1.08	17	1.57	13	3.13	10	[b]		2.06	18
9.98	0.20	82	< 0.28		1.14	21	< 0.96		1.37	27
10.09	1.92	11	2.35	10	2.89	11	2.61	21	2.49	16
10.45	0.59	30	< 0.16		0.31	69	1.45	36	1.79	29
10.81	3.55	9	4.67	7	3.52	10	3.20	18	6.39	9
10.90	1.18	19	1.55	13	2.33	12	[a]		3.11	14
11.16	4.43	8	5.10	7	9.07	7	13.86	8	6.49	9
11.50	0.23	81	0.16	90	1.10	22	< 1.01		0.57	64
11.65	3.96	9	2.97	8	5.11	8	9.02	9	6.34	9
11.88	1.11	20	1.14	15	0.62	38	1.70	25	6.34	9
12.03	< 0.93		1.41	35	< 1.04		1.60	88	3.10	37
12.19	1.04	21	1.15	15	1.64	16	< 1.19		2.05	21
12.65	[a]		0.30	57	0.84	28	1.92	35	1.72	23
12.98	< 0.31		< 0.34		0.62	42	0.84	88	< 0.85	
13.41	3.25	9	2.07	12	2.48	13	4.78	16	3.81	13
13.78	1.70	14	1.61	13	2.38	14	[a]		1.76	24
13.97	1.79	13	1.48	15	2.31	14	1.83	38	2.40	19
14.45	0.38	52	0.77	28	1.49	21	[b]		< 0.60	
14.77	0.85	24	1.31	16	1.01	28	[b]		0.59	69

[a] Unable to extract cross section here.
[b] Outside range of spectra.

TABLE XIII. Cross sections (fm^2/sr) and uncertainties (%) for transitions in ^{34}S. Upper limits are given for cases with large uncertainties.

	Incident energy E_0 (MeV)									
E_x	56.5		54.6		45.7		34.9		56.5, 149°	
(MeV)	$10^7\sigma$	$d\sigma$ (%)	$10^7\sigma$	$d\sigma$ (%)	$10^7\sigma$	$d\sigma$ (%)	$10^7\sigma$	$d\sigma$ (%)	$10^7\sigma$	$d\sigma$ (%)
9.48	1.40	16	2.39	9	3.34	10	[b]		[b]	
9.87	0.73	52	<0.45	[a]	1.57	35	1.65	54	1.15	76
10.00	0.63	25	0.49	30	1.56	12	0.50	85	1.22	33
10.18	0.54	28	0.86	18	2.59	9	6.12	9	0.56	33
10.43	1.21	15	0.69	26	0.73	24	2.15	22	2.48	20
10.66	0.96	17	1.55	12	0.97	17	1.44	30	1.90	21
10.80	0.78	21	0.86	20	1.83	11	2.94	15	< 0.66	
11.02	0.87	19	0.71	23	0.63	25	0.95	19	2.13	21
11.35	0.33	52	0.41	39	1.68	12	1.73	25	< 0.73	
11.50	[a]		[a]		1.49	13	3.26	14	1.78	23
12.12	0.91	28	1.38	19	1.40	21	1.86	14	2.69	22
12.18	1.89	14	1.50	16	1.51	18	2.48	11	2.56	13
12.46	0.58	47	0.88	30	1.22	25	<1.39	[a]	1.96	30
12.66	1.25	16	2.10	10	3.15	8	3.40	15	3.90	12
12.93	0.51	37	0.71	27	0.82	23	[a]		1.57	26
13.59	1.86	14	1.15	20	1.52	15	0.64	85	1.40	30
13.79	0.85	25	0.19	97	[a]		0.45	44	[a]	
13.99	0.47	45	0.67	31	0.68	30	1.75	34	[a]	
14.20	[b]		0.74	28	0.72	28	[b]		1.24	32
14.32	0.45	47	2.02	12	0.97	21	[b]		2.81	15
14.43	1.17	20	1.26	18	1.64	14	[b]		1.64	31
14.80	3.55	9	3.65	8	4.02	8	[b]		2.32	18

[a] Unable to extract cross section here.
[b] Outside range of spectra.

an excitation energy of 15 MeV to match the maximum excitation energy studied in this experiment. The "free-nucleon" shell-model predictions are in good agreement with the Kurath sum rule, while the experimental energy-weighted sums are in better agreement with results from effective-operator shell-model calculations as found earlier with non-energy-weighted sums (see Table IX).

Measured $M2$ transitions are listed in Tables I–III. Figures 11 and 12 show the $M2$ strength distributions in ^{30}Si, ^{32}S, and ^{34}S. The summed $M2$ strengths $\sum B(M2)$ for ^{30}Si, ^{32}S, and ^{34}S are $(348 \pm 86)\mu_N^2$ fm^2, $(247 \pm 73)\mu_N^2$ fm^2, and $(233 \pm 50)\mu_N^2$ fm^2, respectively. These results are clearly lower limits because more $M2$ strength is expected at higher excitation energies.

VIII. CONCLUSIONS

Low-multipolarity magnetic strengths, especially dipole and quadrupole strengths in the *sd*-shell nuclei ^{30}Si, ^{32}S, and ^{34}S, have been measured in the excitation energy range 9–15 MeV. A large fragmentation is seen in ^{30}Si and ^{34}S, while the strength is concentrated to a greater degree in the self-conjugate nucleus ^{32}S. The sums of experimental $M1$ strengths in all three nuclei are in better agreement with shell-model calculations using an effective $M1$ operator, but appear quenched compared to the shell-model results using free-nucleon operators. A similar observation has previously been made in the cases of ^{36}Ar and ^{38}Ar by Foltz *et al.* [23].

ACKNOWLEDGMENTS

We acknowledge the support of the management and staff of the University of Illinois Nuclear Physics Laboratory for their cooperation throughout all phases of the 180° project. We are grateful to X. Jiang of CUA and W. Kim and M. Leuschner of the University of New Hampshire for their help in the data acquisition. We thank W. Lozowski of the University of Indiana for his help with target preparation. B. A. Brown of Michigan State University provided us with the results of the shell-model calculations. This research was supported in part by National Science Foundation Grants PHY 88-20654, PHY 89-21146, and PHY 91-22139 and in part by the Department of Energy under Contract DE-AC05-84OR21400 with Martin Marietta Energy Systems, Inc.

APPENDIX

Tables XI, XII, and XIII present experimental cross sections obtained for the observed transitions in ^{30}Si, ^{32}S, and ^{34}S.

[1] B. A. Brown and B. H. Wildenthal, Annu. Rev. Nucl. Part. Sci. **38**, 29 (1988).
[2] S. Raman, L. W. Fagg, and R. S. Hicks, in *Electric and Magnetic Giant Resonances in Nuclei*, edited by J. Speth (World Scientific, Singapore, 1991), p. 75.
[3] U. E. P. Berg, K. Ackermann, K. Bangert, C. Bläsing, W. Naatz, R. Stock, K. Weinhard, M. K. Brussel, T. E. Chapuran, and B. H. Wildenthal, Phys. Lett.

140B, 191 (1984).
[4] B. H. Wildenthal, in *Progress in Particle and Nuclear Physics*, edited by D. H. Wilkinson (Pergamon, Oxford, 1984), Vol 11, p. 5.
[5] B. A. Brown and B. H. Wildenthal, Nucl. Phys. **A474**, 290 (1987).
[6] A. Richter, A. Weiss, O. Haüsser, and B. A. Brown, Phys. Rev. Lett. **65**, 2519 (1990).
[7] I. S. Towner and F. C. Khanna, Nucl. Phys. **A399**, 334 (1983).
[8] P. E. Burt, L. W. Fagg, H. Crannell, D. I. Sober, W. Stapor, J. T. O'Brien, X. K. Maruyama, J. W. Lightbody, R. A. Lindgren, and C. P. Sargent, Phys. Rev. C **29**, 713 (1984).
[9] M. Petraitis, Ph.D. dissertation, Catholic University of America, 1993.
[10] J. T. O'Brien, D. I. Sober, L. W. Fagg, Hall Crannell, M. Petraitis, J. P. Connelly, S. E. Williamson, and J. R. Deininger, Nucl. Instrum. Methods A **312**, 531 (1992).
[11] H. Theissen, *Springer Tracts of Modern Physics*, Vol. 65 (Springer, Heidelberg, 1972), p. 1.
[12] M. Rosen, R. Raphael, and H. Überall, Phys. Rev. **163**, 927 (1967).
[13] B. A. Brown, documentation in the program DENS (unpublished).
[14] R. Schneider, A. Richter, A. Schwierczinski, E. Spamer, O. Titze, and W. Knüpfer, Nucl. Phys. **A323**, 13 (1979).
[15] W. Gross, D. Meuer, A. Richter, E. Spamer, O. Titze, and W. Knüpfer, Phys. Lett. **84B**, 296 (1979).
[16] P. E. Burt, L. W. Fagg, H. Crannell, D. I. Sober, W. Stapor, J. T. O'Brien, X. K. Maruyama, J. W. Lightbody, and R. A. Lindgren, Phys. Rev. C **25**, 2805 (1982).
[17] P. M. Endt, Nucl. Phys. **A521**, 1 (1990).
[18] W. Gross, Ph.D. Diplomarbeit, Institut für Kernphysik, Technische Hochschule, Darmstadt, 1981.
[19] R. Benz, Ph.D. Diplomarbeit, Institut für Kernphysik, Technische Hochschule, Darmstadt, 1984.
[20] B. A. Brown (private communication).
[21] D. I. Sober, B. C. Metsch, W. Knüpfer, G. Eulenberg, G. Küchler, A. Richter, E. Spamer, and W. Steffen, Phys. Rev. C **31**, 2054 (1985). These authors use the multiplicative factor of $\frac{9}{28\pi}$ for the $f_{7/2} \rightarrow f_{5/2}$ transition.
[22] D. Kurath, Phys. Rev. **130**, 1525 (1963).
[23] C. W. Foltz, L. W. Fagg, D. I. Sober, H. D. Gräf, A. Richter, E. Spamer, and B. A. Brown, Phys. Rev. C **49**, 1359 (1994).

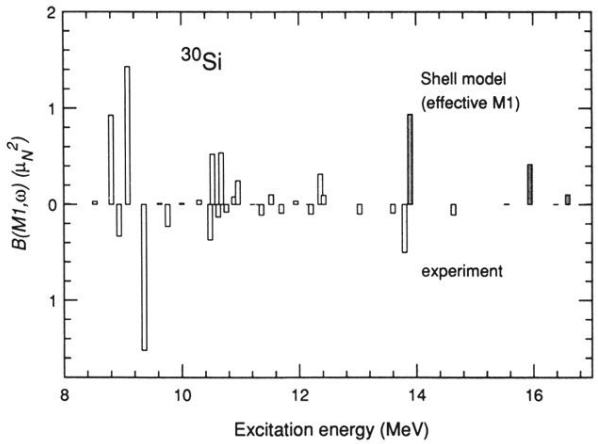

FIG. 5. Comparison of shell-model and experimental strengths for ^{30}Si. The shaded bars in the shell-model strengths indicate $\Delta T = 1$ transitions and the unshaded bars represent $\Delta T = 0$ transitions.

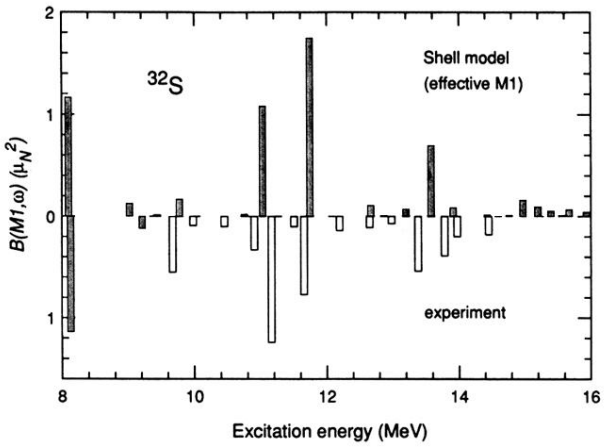

FIG. 6. Comparison of shell-model and experimental strengths for ^{32}S. The shaded bars in the shell-model strengths indicate $\Delta T = 1$ transitions. The shaded bars in the experimental strengths represent data from Refs. [3,8]. The unshaded bars are experimental results from the current work.

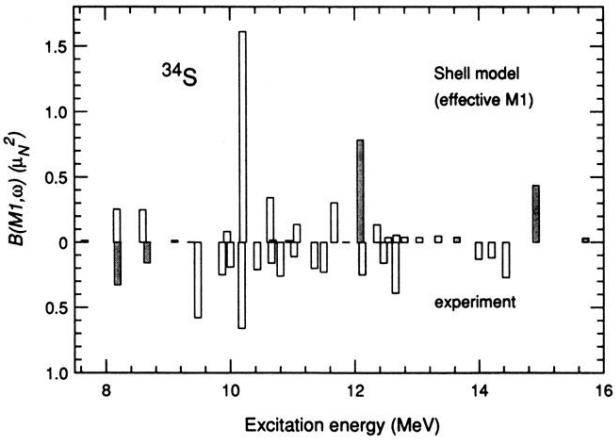

FIG. 7. Comparison of shell-model and experimental strengths for ^{34}S. The shaded bars in the shell-model strengths indicate $\Delta T = 1$ transitions and the unshaded bars represent $\Delta T = 0$ transitions. The shaded bars in the experimental strengths represent data from from Ref. [3]. The unshaded bars are experimental results from the current work.